



Liquid water transport mechanism in the gas diffusion layer

P. Zhou, C.W. Wu*

State Key Laboratory of Structure Analysis for Industrial Equipment, Department of Engineering Mechanics, Faculty of Vehicle Engineering and Mechanics, Dalian University of Technology, Dalian 116024, PR China

ARTICLE INFO

Article history:

Received 30 June 2009

Received in revised form 8 September 2009

Accepted 9 September 2009

Available online 28 September 2009

Keywords:

Gas diffusion layer

Water management

Liquid water configuration

ABSTRACT

We developed an equivalent capillary model of a microscale fiber-fence structure to study the microscale evolution and transport of liquid in a porous media and to reveal the basic principles of water transport in gas diffusion layer (GDL). Analytical solutions using the model show that a positive hydraulic pressure is needed to drive the liquid water to penetrate through the porous GDL even consisting of the hydrophilic fibers. Several possible contributions for the water configuration, such as capillary pressure, gravity, vapor condensation, wettability and microstructures of the GDL, are discussed using the lattice Boltzmann method (LBM). It is found that the distribution manners of the fibers and the spatial mixed-wettability in the GDL also play an important role in the transport of liquid water.

© 2009 Elsevier B.V. All rights reserved.

1. Introduction

Owing to the high efficiency, low noise, and minimal pollution, the proton exchange membrane (PEM) fuel cell has emerged as one of the most promising power sources for the automobile engine. Gas diffusion layer (GDL) is one of the essential components of the PEM fuel cells. The main roles of the GDL are to allow the gaseous reactants (oxygen in cathode and hydrogen in anode) to move towards the catalyst layer (CL) or the micro-porous layer (MPL) and to provide paths for liquid water to flow towards the flow channel. It also plays an important role in the electron and thermal transports. If a large number of pores were blocked by the liquid water in the GDL the number of the available pores for gaseous flow would decrease. Therefore the gaseous flow resistance will increase and the effective reaction area will reduce in the CL. Control of the liquid water distribution (the water management technology), a key technique to ensure high performance and long durability of PEM fuel cells, has received much attention. An effective water management requires a careful design of the GDL microstructure, such as the porosity, the pore size distribution, and the spatial mixed-wettability distribution.

Understanding the fundamental mechanisms of water transport in the GDL is a key step for the effective management of liquid water. The capillary pressure and vapor condensation are considered as two of the main contributors to the water configuration. Generally, liquid water transport in a porous media is governed by the capillary fingering. It is necessary to apply a pressure to force

the liquid water to penetrate into the pores of GDL. Therefore, the capillary pressure vs. liquid water saturation curve, providing a constitutive relationship to simulate the liquid water transport in the cathode, has received considerable attention [1,2]. However, recent studies show that the vapor condensation obviously affects the liquid water transport in the cathode [3–5], i.e., the capillary pressure driven flow is not the only physical phenomenon in cathode.

Both experimental observations [4,5] and numerical simulation [3] show that the vapor condensation (liquid–vapor phase change) plays a pivotal role in the water configuration. The vapor condensation is affected by the temperature difference in the GDL and the local wettability. The liquid water configuration dominated by phase change differs completely from that dominated by the capillary pressure driven flow. If it is completely dominated by capillary pressure, the liquid water will flow from the higher saturation region (GDL–MPL interface) to the lower saturation region (GDL–channel interface) because a large capillary pressure is given in the high saturation region. Continuous liquid water flow in micro-pores, one of the basic assumptions in capillary pressure driven flow in porous media, is never observed *in situ* in a PEM fuel cell system. On the contrary, a series of discrete small droplets in the GDL are often observed using the environmental scanning electron microscope (ESEM) [6,7]. Although the transport process in the GDL cannot be clearly observed *in situ* in a PEM fuel cell system, it can be verified that the liquid water in the GDL is discrete even when the water droplets intrude into the gas flow channel [4,5,8]. This is inconsistent with the basic assumption of capillary pressure driven flow. Therefore, the phase change may be another key factor to affect the liquid water configuration besides the capillary pressure. ESEM imaging [6,7] and synchrotron X-ray radiography [4,5] provide a high spatial resolution technique to investigate droplet

* Corresponding author. Tel.: +86 0411 84706353; fax: +86 0411 84706353.
E-mail address: cwwu@dlut.edu.cn (C.W. Wu).

formation at the microscale, however, the ability to simulate fuel cell operating conditions has not yet been reported in the literature [9].

The hydrophobic treatment technology [10] for the GDL fibers can reduce the hydrophilic regions where the vapor condensation easily occurs. However, the hydrophobic treatment increases the hydraulic pressure for driving the liquid water flow through the micro-pores. It has been shown that an appropriate content of Teflon (5–30 wt%) in the GDL can increase the performance of PEM fuel cell [10–12]. There are some other factors controlling the liquid configuration besides the fraction of the hydrophobic fibers (e.g., fibers coated with Teflon), for example, the non-uniform distribution of the hydrophobic fibers discussed by Sinha and Wang [13]. It is generally accepted that a higher pressure is required to push the water through a hydrophobic GDL than through a hydrophilic GDL [14], and the liquid water preferentially flows through the connected hydrophilic pore network of a mixed-wet GDL [13]. This paper will study the quantitative relationship between the liquid water transport resistance and the pore properties in the GDL, including the geometry parameters and wettability.

2. Analysis methods

The gas diffusion layer is generally made of either a woven carbon cloth or a nonwoven carbon paper. It has usually been modeled as a homogeneous porous medium with a constant permeability in the published literatures of PEM fuel cells [15–17]. The methods used in those literatures show a high numerical efficiency since they do not require very fine grid to capture the microstructure of the GDL. However these macroscopic models fail to take into account the influence of the local wettability and structural morphology which affect the cell performance [18]. In fact, most of the GDLs are not homogeneous. For a carbon cloth GDL, the size of the carbon fiber bundle is about 200 μm, close to the thickness of the GDL (~300 μm). For a carbon paper GDL, the largest pore size reaches over 100 μm, also close to the thickness of the GDL [1,19,20]. According to the experimental observation [14], the unsaturated flow in the GDL is affected by the wettability of the local fiber surface, the pore size distribution, and the fiber diameter, etc. A simplified model is here proposed to study the effects of capillary pressure, gravity, vapor condensation speed, wettability

and microstructures of the GDL on the liquid configuration. Both the analytical and LBM models are adopted in the analysis.

2.1. Analytical method

The analytical analysis is based on the Young–Laplace law, which gives the relationship of the pressure difference across the liquid–gas interface, the interface shape and surface tension:

$$\Delta P = \gamma\kappa = \frac{\gamma}{R_d} \tag{1}$$

where ΔP is the pressure difference across the fluid interface, γ is the surface tension, κ is the curvature of the interface, and R_d is the curvature radius of liquid–gas interface.

The difference of gas and liquid pressure within a porous medium, i.e., the capillary pressure, is balanced by the tension of the liquid–gas interface in the pores. In the previous studies, the GDL pores are often idealized as the equivalent cylindrical capillaries (usually called equivalent cylindrical capillary model) [21]. Based on the Young–Laplace law, the relationship between capillary pressure and equivalent pore size is described as:

$$P_c = P_l - P_g = -\frac{2\gamma \cos(\theta)}{R_p} \tag{2}$$

where R_p is the pore radius, P_l is the pressure of liquid phase, P_g is the pressure of gas phase, θ is the contact angle of liquid water on the fiber surface.

Based on the equivalent cylindrical capillary model, a zero capillary pressure indicates that all the pores are filled with liquid for a hydrophilic GDL, but all the pores are drained for a hydrophobic GDL. However, to the best of our knowledge, the phenomenon that liquid water is imbibed into the GDL without a pressure gradient is never observed in the experiment. In the present paper, we proposed an equivalent capillary model of fiber-fence structure to expound the fundamental mechanisms of liquid water transport in the GDL (see Fig. 1). The continuous solid wall in the equivalent cylindrical model [21] is here replaced by the microscale fiber-fence structure. Since liquid water transports in a quasi-static process at low values of Capillary number and Reynolds number, the dynamic effect is not considered in the analytical analysis. According to the Young–Laplace law and the geometry relationship between the

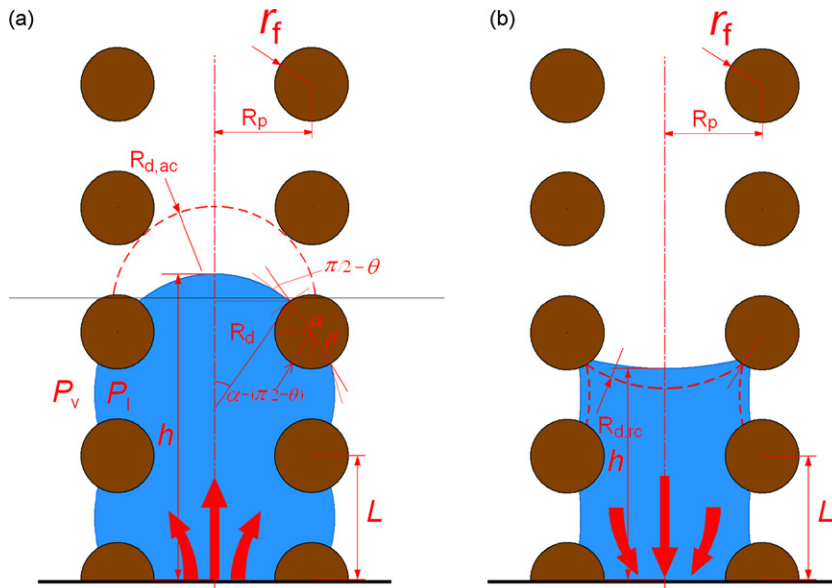


Fig. 1. Schematic of the equivalent capillary model of the fiber-fence structure.

carbon fibers and the liquid–gas interface, the gas–liquid interface profile is obtained (see Fig. 1):

$$R_d = \frac{r_f \cos(\alpha) - R_p}{\cos(\alpha + \theta)} \quad (3)$$

$$h = R_d[1 - \sin(\alpha + \theta)] + r_f \sin(\alpha) + nL \quad (4)$$

where θ is the contact angle of the liquid water on the fiber surface, $2R_p$ the width of the capillary tube, r_f the radius of the fiber, n the fiber layer number that the water surface reaches (equaling 2 in the condition as shown in Fig. 1), L the distance of two neighboring layer fibers, h the center height of the liquid level. The pore size $2R_p$ must be greater than the fiber distance $L - 2r_f$, otherwise, a side leakage of the liquid water may occur between the two neighboring fibers.

During the liquid surface imbibition (rising as shown in Fig. 1a), a transition occurs when the liquid surface touches the inner-bottom surface of the upper layer fibers. But during the liquid surface drainage process (going down as shown in Fig. 1b), the transition occurs when the liquid surface almost leaves the inner-bottom surface of the touching layer fibers. Here we defined an advancing critical radius in the imbibition process, $R_{d,ac}$, equaling the curvature radius of the liquid water surface at the transition point (Fig. 1a). During the drainage process, a receding critical radius, $R_{d,rc}$, occurs when the contact line is just separated from the fiber surface (Fig. 1b). In these two critical conditions, the geometrical relationships are given as follows:

$$[(h_{ac} - R_{d,ac}) - (n + 1)L]^2 + R_p^2 = (R_{d,ac} + r_f)^2 \quad (5)$$

$$\alpha_{rc} + \beta_{rc} = -\frac{\pi}{2} \quad (6)$$

where the subscripts ac and rc denote the advancing critical value and receding critical value respectively.

From Eq. (3), one obtains:

$$\frac{\partial R_d}{\partial \alpha} = \frac{r_f \sin(\theta) - R_p \sin(\alpha + \theta)}{\cos^2(\alpha + \theta)} \quad (7)$$

When $\partial R_d / \partial \alpha = 0$, i.e.,

$$r_f \sin(\theta) - R_p \sin(\alpha + \theta) = 0 \quad (8)$$

combining Eqs. (2) and (3), the minimum curvature radius and the corresponding maximum capillary pressure are obtained. The maximum capillary pressure is just the hydraulic pressure required for the liquid water to penetrate into the GDL.

2.2. Multiphase lattice Boltzmann method

In the above section, we propose an analytical method to analyze the transport of liquid water in the GDL induced only by the capillary pressure. In the present section, we will use the lattice Boltzmann method (LBM) [22], to study the transport of liquid water in the GDL when the vapor condensation and stochastic microstructure are considered. The LBM has been accepted as a new computational tool for two-phase flow with phase change in complex geometries, and has been used for simulating the liquid water in the GDL in order to obtain a fundamental understanding [23–27]. Here we use the multiphase and single-component LBM originally proposed by Shan and Chen (SC) [28] to simulate the water flow in the porous GDL. The SC multiphase LBM used a concept of the microscopic interactions between the fluid particles at the neighboring lattices by adding the additional forcing term to the velocity field. The interaction force is controlled by the equation of state (EOS). The spurious currents (the unphysical velocities generated in the simulation) are ubiquitous in the SC model and cannot be separated from the real flow velocities. Yuan and Schaefer [29] discussed some choices of EOS and proposed that the P–R

(Peng–Robinson) EOS [30] gives a better result with low spurious currents.

In this paper, the computation code of the SC LBM was designed by us and was validated through careful comparisons with the analytical results of the equivalent capillary model of fiber-fence structure. Here, we implement the SC LBM in two-dimension flow analysis for a single-component multiphase flow system. In the D2Q9 (two-dimension and nine discrete velocities) model, a standard LBM with the BGK (Bhatnagar–Gross–Krook) collision term is adopted, describing the evolution of particle distribution function (PDF) f_i in site \mathbf{x} and time t as follows:

$$f_i(\mathbf{x} + \mathbf{e}_i \delta t, t + \delta t) = f_i(\mathbf{x}, t) - \frac{1}{\tau} [f_i(\mathbf{x}, t) - f_i^{\text{eq}}(\mathbf{x}, t)], \quad (9)$$

$$i = 0, 1, 2, \dots, 8$$

where δt is the time step, subscript i indicates the discrete velocity direction. τ is the single relaxation time, having the relation with the kinematic viscosity: $\nu = (\tau - 0.5)c_s^2 \delta t$, $c_s = c/\sqrt{3}$, where $c = \delta x / \delta t$ is the ratio of lattice spacing δx and time step δt . f_i^{eq} is equilibrium PDF, and can be calculated as

$$f_i^{\text{eq}}(\mathbf{x}, t) = \omega_i \rho \left[1 + \frac{\mathbf{e}_i \cdot \mathbf{u}^{\text{eq}}}{c_s^2} + \frac{(\mathbf{e}_i \cdot \mathbf{u}^{\text{eq}})^2}{2c_s^4} - \frac{(\mathbf{u}^{\text{eq}})^2}{2c_s^2} \right], \quad (10)$$

$$\omega_i = \begin{cases} 4/9, & i = 0 \\ 1/9, & i = 1-4 \\ 1/36, & i = 5-8 \end{cases}$$

In Eqs. (9) and (10), \mathbf{e}_i is the discrete velocities, given by

$$\mathbf{e} = c \cdot \begin{bmatrix} 0 & 1 & 0 & -1 & 0 & 1 & -1 & -1 & 1 \\ 0 & 0 & 1 & 0 & -1 & 1 & 1 & -1 & -1 \end{bmatrix} \quad (11)$$

The macroscopic density and the modified macroscopic velocity are given as follows:

$$\rho = \sum_i f_i \quad (12)$$

$$\mathbf{u}^{\text{eq}} = \frac{\sum_i f_i \cdot \mathbf{e}_i + \tau \cdot \delta t \cdot \mathbf{F}}{\rho} \quad (13)$$

In the single-component multiphase LB model proposed by Shan and Chen, a simple long-range interaction force between the particle at site \mathbf{x} and the particle at site \mathbf{x}' is introduced as:

$$\mathbf{F}(\mathbf{x}) = \frac{\psi(\mathbf{x}) \sum_{\mathbf{x}'} \omega_i \psi(\mathbf{x}') (\mathbf{x}' - \mathbf{x})}{c_s^2} \quad (14)$$

where $\psi(\mathbf{x})$ is called the “effective mass” or “pseudo potential function” and is defined as a function of \mathbf{x} as:

$$\psi(\mathbf{x}) = \sqrt{2(\rho(\mathbf{x})c_s^2 - p(\rho(\mathbf{x})))} \quad (15)$$

The pressure p of non-ideal gas is described by the EOS.

The single-component multiphase LB model is often limited to a small density ratio because numerical instability may appear in case of a large density ratio. Yuan and Schaefer [29] discussed some choices of EOS and proposed that the P–R EOS gives better results in cases of large density ratio. The pressure of non-ideal gas is described by the P–R EOS as:

$$p = \frac{\rho RT}{1 - b\rho} - \frac{a\alpha(T)\rho^2}{1 + 2b\rho - b^2\rho^2} \quad (16)$$

$$\alpha(T) = \left[1 + (0.37464 + 1.54226\omega - 0.26992\omega^2) \times \left(1 - \sqrt{T/T_c} \right) \right]^2 \quad (17)$$

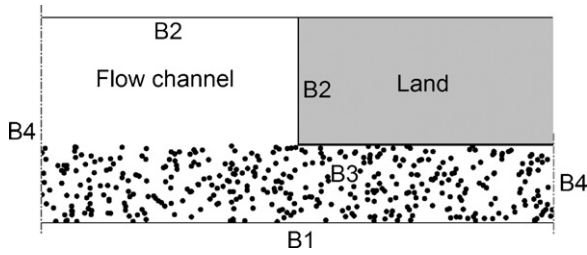


Fig. 2. Schematic of the calculation region and boundary conditions.

where $a = 0.445724R^2T_c^2/p_c$, $b = 0.08778RT_c/p_c$, T_c is the critical temperature, p_c is the critical pressure, $R = 1$ in the present simulation, ω is the acentric factor equaling 0.344 for water [29].

The wetting phenomena of the liquid–solid interface can be implemented by appointing a pseudo effective mass ψ_w to simulate the interaction force (similar to the fluid–fluid interaction [31]) at the fluid–solid boundary. The wetting property of the solid boundary is given by adjusting the ψ_w from ψ_g (effective mass of gas phase) to ψ_l (effective mass of liquid phase).

The analysis region is shown in Fig. 2. Similar to the homogenous macroscopic 2D model [32,33], it contains the flow channel and GDL. Boundary B4 is treated as a symmetric boundary, B1 is the interface of the GDL and MPL, B2 is the surface of the bipolar plate, and B3 is the surface of the fibers. The MPL is treated as a boundary in the model. No-slip boundary condition is used at B1, B2, and B3. The diameter of the carbon fiber is 10 μm , and the porosity is $\sim 80\%$, which is close to the real porosity of Toray TGP-H carbon paper. The width of the analysis region is 1 mm, and thickness of the GDL is 150 μm . The lattice spacing δx equals 0.5 μm . At the initial step, the carbon fibers are placed either randomly or regularly, while the whole region is occupied by the saturated vapor. Due to the water-free spots caused by the Teflon, the water in the MPL appears in the form of vapor. Source terms (denoting the vapor diffused into the GDL from MPL) are added to the evolution equations of the lattices at B1. The water content increases continuously with a very small velocity. When the liquid water droplet intrudes into the channel and becomes big enough, it is blown away along the channel. In the simulation process in the simplified 2D model, the water droplet in the channel is cleared away instantaneously. However, how the droplet to move away after its formation in the channel is out of the scope of the present paper.

In the LBM analysis, the water contact angle of the bipolar plate is assumed to be 80° [34], and the contact angle of the MPL surface (B1 in Fig. 2) is assumed to be 150° [35]. As for the wettability of the fibers in the GDL, a contact angle of 110° corresponds to the carbon fibers coated by Teflon, but a contact angle of 80° corresponds to the untreated carbon fibers [36].

We use a constant pore size distribution model (i.e., the GDL consists of uniformly arrayed fibers) to analyze the effect of the mixed-wettability, but use the random pore size distribution model to analyze the process of liquid water removal from the MPL to the flow channel. The effect of pore size distribution is here discussed qualitatively, such as regular distribution and random distribution.

3. Results and discussion

3.1. Capillary pressure driven flow in porous media

Based on the equivalent capillary model of fiber-fence structure, the curvature radius of the liquid–gas interface is determined from Eqs. (3) and (4). For each calculation point, the transition condition is judged by Eq. (5). When Eq. (5) is satisfied, the variable n will be increased by 1 in Eq. (4). The volume of the liquid water is assumed unchanged before and after jumping of the water surface. The cur-

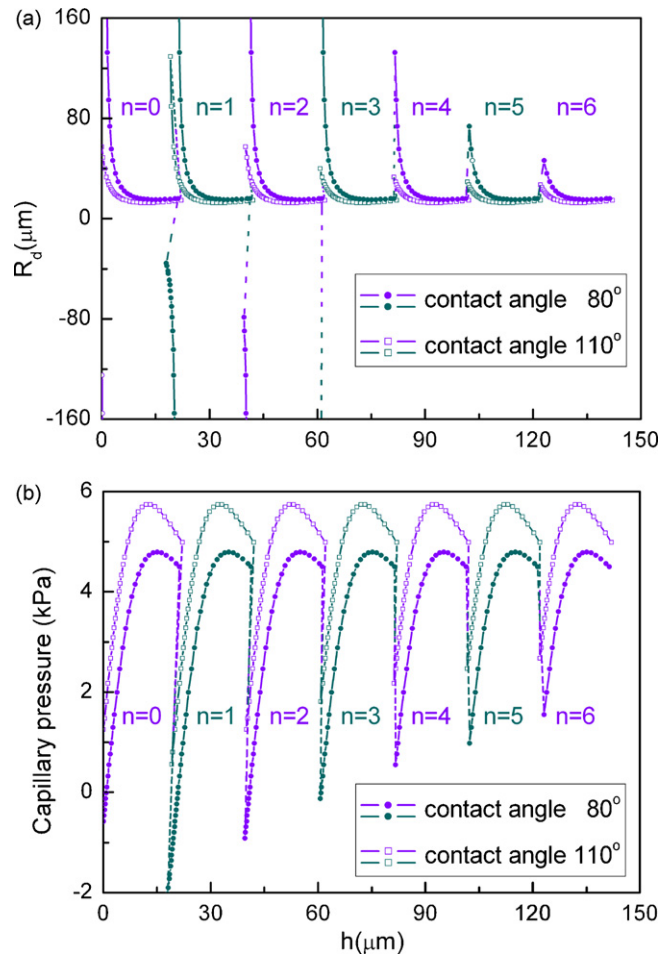


Fig. 3. The liquid surface property vs. the height of the liquid surface for different wettabilities of the fiber surfaces in the imbibition process. (a) The curvature radius and (b) the capillary pressure. $L = 20 \mu\text{m}$ and $R_p = 15 \mu\text{m}$. The dashed line expresses the transition process in which the liquid–gas interface touches the inner-bottom surface of upper layer of the fibers. n denotes the fiber layer number that the water surface reaches.

vature radii of the liquid–gas interface are shown in Fig. 3a when the liquid water gradually intrudes into the upper fiber layers in the imbibition process. The change of the curvature radius of the liquid surface shows approximately a periodical behavior except at the regions nearby the transition points. When n is less than 3 and the fibers are hydrophilic, the curvature radius will become a negative value, i.e., the liquid–gas interface is concave. However, the curvature is always positive when the fibers are hydrophobic. Except at the regions nearby the transition points, the influence of the fiber wettability on the curvature radius is not as large as expected.

The corresponding capillary pressures predicted by Eq. (1) are shown in Fig. 3b. The curves show a periodic behavior and there is a maximum capillary pressure in each period. To drive the liquid water going through the capillary pore, a hydraulic pressure should be applied to overcome the maximum capillary pressure. When the contact angle of the fiber surface is changed from 80° to 110° , the maximum capillary pressure is increased from 4.79 kPa to 5.74 kPa. However, based on Eq. (2), the equivalent cylindrical model gives the corresponding equivalent contact angles of 120° and 127° respectively. Therefore, all of these pores belong to hydrophobic pores according to the equivalent cylindrical model. The maximum capillary pressure is always positive even when the contact angle is 60° as shown Fig. 4. The maximum capillary pressure is greater than 1.7 kPa when the width ($2R_d$ as shown in Fig. 1) of the capillary pore ranges from 20 μm to 80 μm and the contact

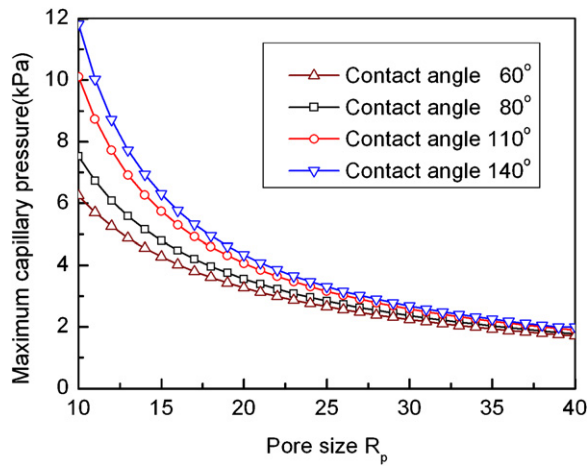


Fig. 4. The maximum capillary pressure to drive the liquid water flowing through the pores. $L = 20 \mu\text{m}$.

angle ranges from 60° to 110° . Therefore, the liquid water would not intrude into the GDL without an applied hydraulic pressure if the phase change and the gravity are both negligible. In fact, the maximum capillary pressure is always positive. Now let us discuss the limiting situation. For the completely wetting (zero contact angle) fibers, the water surface curvature is zero when the height of the liquid surface equals $nL + r_f$. Then, the curvature is positive with the increase in the height of the liquid surface before the liquid surface touches the next layer of fibers (i.e., a surface jumping occurs). The jumping phenomenon in the capillary pressure is speculated as a special phenomenon occurring in the fiber porous media.

The equivalent capillary model of fiber-fence structure can be used to reveal the mechanism of the liquid water transport in the GDL induced by capillary pressure. But effects of the phase change and the body force cannot be included in the analytical solution. Therefore, a numerical solution for the LBM will be carried out in the following analysis to study the effects of gravity and phase change, and the transport process of water. The analytical and LBM solutions based on the equivalent capillary model of fiber-fence structure are compared in Fig. 5a and b for the different fiber wettabilities. In Fig. 5a we give the comparison between the analytical solution and LBM solution for a large range of water level height (5 layers of fibers) when the contact angle $\theta = 80^\circ$. In Fig. 5b we give a detailed comparison of the analytical solutions and the LBM solutions for $\theta = 60^\circ, 80^\circ, 110^\circ$ and 140° respectively at the first two layers of fibers. Good agreements occur between the LBM simulations and the analytical solutions except at the regions nearby the transition points. The LBM simulation shows a quasi-static process of the liquid surface elevation, but the analytical solution gives a completely static process.

3.2. Gravitational effect

The Bond number (denoted here by B_0), a dimensionless number expressing the ratio of the body forces to the surface tension force, is expressed as:

$$B_0 = \frac{\rho g l^2}{\gamma} \quad (18)$$

where ρ is the density of the liquid, g the gravity acceleration, l the characteristic length (the radius of a droplet or the radius of a capillary tube), γ the surface tension of the interface. When the droplet radius is $100 \mu\text{m}$ in the GDL, the Bond number is about 0.0015. Therefore, effect of the gravity on the capillary flow in the GDL is very small and is not considered in the present paper. However,

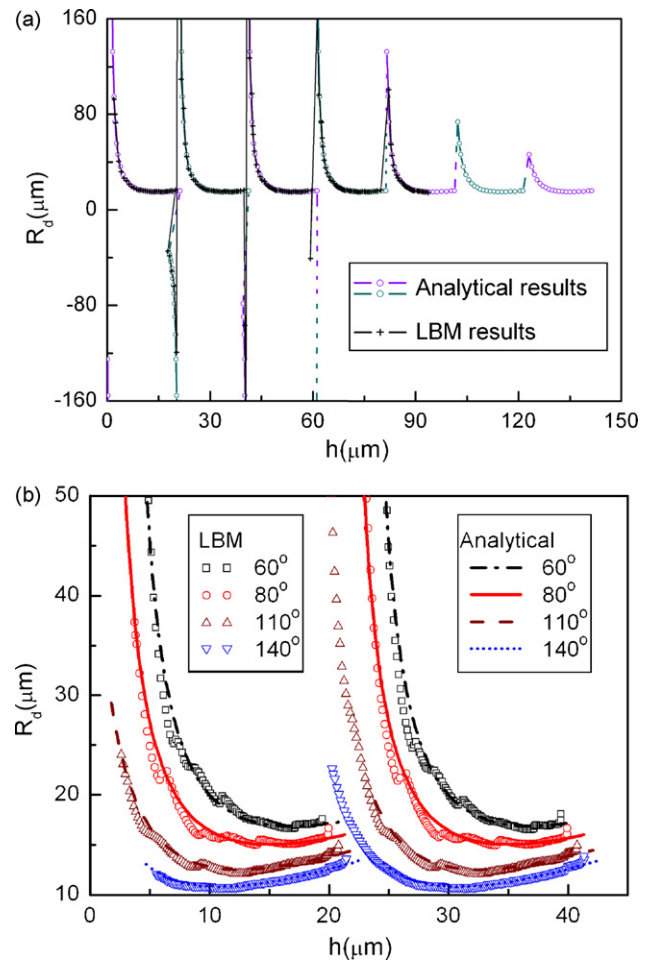


Fig. 5. Comparison between the analytical solution and the LBM simulation for the surface curvature radius of the liquid water for different contact angles as indicated in the figures ($L = 20 \mu\text{m}$ and $R_p = 15 \mu\text{m}$): (a) the analytical solution and LBM method for contact angle $\theta = 80^\circ$ for a large range of water level height and (b) the detailed comparison of the analytical solution and the LBM solutions for $\theta = 60^\circ, 80^\circ, 110^\circ$ and 140° respectively at the first two layers of fibers.

the largest droplet intruding in the gas flow channel will be greater than 1 mm , and the corresponding Bond number is greater than 0.136. In this case, the gravity may affect the water droplet configuration and detachment. The performance of the PEM fuel cell is gravity-dependent as observed by Kimball et al. [37].

3.3. Effect of vapor condensation

The water removal induced by vapor condensation (or phase change) is affected by the wettability of GDL fibers, the vapor diffusion velocity, and the temperature gradient. The temperature effect is not considered in the present study due to the limitation of SC LBM despite a little temperature difference ($\sim 3 \text{ K}$) may have obvious effect on the water distribution as reported in Ref. [3]. Up to now, the single-component multiphase SC LBM still cannot simulate the situation at low temperature ($< 373 \text{ K}$) and high density ratio due to the numerical instability at large density ratio. The temperature studied in the present paper is $0.8T_c$ ($T_c = 647 \text{ K}$). Therefore, the analysis for the phase change process is qualitative.

When the vapor condensation effect is considered in the LBM model, the liquid water distribution is dominated by the vapor diffusion velocity and the water production rate. Fig. 6 shows the liquid water distribution for several values of the source terms when the average liquid water saturation in the GDL is $\sim 15\%$. The

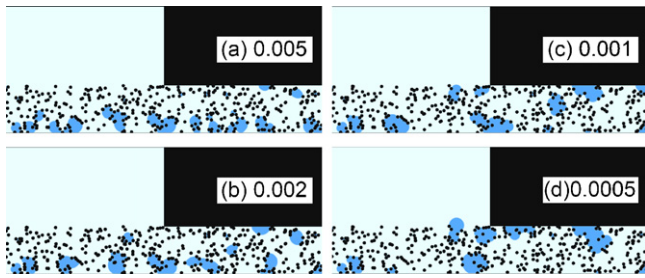


Fig. 6. The liquid water configuration for different source terms: (a) 0.005, (b) 0.002, (c) 0.001, and (d) 0.0005. All the fibers are hydrophilic and give a random distribution. The blue regions denote the liquid water droplets. (For interpretation of the references to color in this figure legend, the reader is referred to the web version of the article.)

source terms are 0.005, 0.002, 0.001, and 0.0005 respectively for each time step. A large velocity of phase change occurs where the vapor pressure is high. Due to the flow and diffusion resistances, the vapor pressure near the MPL–GDL interface (B1) is higher than that at the top surface of the GDL, and therefore the vapor will condense at the small pores near B1. Generally, the small pores are surrounded by more carbon fibers than the large pores, and thus give more hydrophilic property than the large pores. When the source term is reduced, the pressure difference between the top and bottom regions will decrease due to the abundant time for vapor diffusion. Therefore, the condensation occurs at the whole GDL region but not only at the region near B1. Based on the LBM simulations for different source terms, we found that the two main positions of liquid water condensation are located close to the interface of the rib land and the MPL–GDL interface (B1). This is supported by the experimental observations [4,5] and numerical simulation [3]. Even though the temperature effect is not considered, the present simulation shows that a hydrophilic land surface can easily induce the vapor condensation occurring under the land. This agrees with the experimental observations [4,5] although the physical reasons in the experiments may contain the temperature effect. Due to little physical basis of the phase change velocity in the SC LBM model, the source term is still difficult to be translated in to real world units. The current density is $3.72 \times 10^{-5} / \delta t$ (Ccm^{-2}) when the value of the source term is 0.001 (If the time step is $0.5 \mu\text{s}$, the current density is 74.4 Acm^{-2}). The real time step is

still difficult to be given due to unreal phase change velocity in the model.

3.4. Liquid water formation and transport

What is discussed above shows that the capillary driven flow and phase change are the two main physical principles of the water transport in GDL. Here we will analyze the transport process of the liquid water from MPL towards the flow channel and the effect of the spatial mixed-wettability distribution on the liquid water configuration.

Fig. 7(a)–(f) shows the liquid water configuration when the carbon fibers distribute regularly but have different surface wettabilities. The average saturation in the GDL is 45%, and the porosity is $\sim 80\%$. The insets at the top right corners (lands) in the figures show the fiber distribution types: (a) all the fibers are hydrophilic; (b) all the fibers are hydrophobic; (c)–(f) the hydrophobic fiber fraction is taken as a constant (50%), but the hydrophobic and hydrophilic regions are different. The black dots denote the hydrophilic fibers, while the orange dots denote the hydrophobic fibers. In such a case, we found that the liquid water distribution is completely different. Therefore, the fraction of hydrophobic fibers cannot itself describe the transport ability of the liquid water through the GDL. The difference of the maximum pressure between the hydrophilic and hydrophobic pores induces the liquid water preferentially flowing into the hydrophilic pores. The hydrophobic fibers surrounding the hydrophilic regions give a large resistance to the liquid water flow. The fiber distribution patterns shown in Fig. 7(d) and (f) seem more efficient for the water management and the cell efficiency since the gas paths in the GDL are not hindered by the liquid water. The liquid water easily congregates at the land–GDL interface due to the hydrophilic surface of the land (see Fig. 7(a)–(d)). The aforementioned analysis is carried out based on the assumption of regularly distributed carbon fibers.

Fig. 8(a)–(d) shows the liquid water configuration for different average saturations. In Fig. 8 all the fibers are hydrophilic. The process of liquid water transport from the MPL to the GDL can thus be summarized as follows: initially, the liquid water condenses at the small pores, then some of the water droplets grow up, but others may either stop growing up or go off. Once they grow up to big enough to touch more hydrophilic fibers, they will never vanish. After they are surrounded by too many fibers the droplets will stop

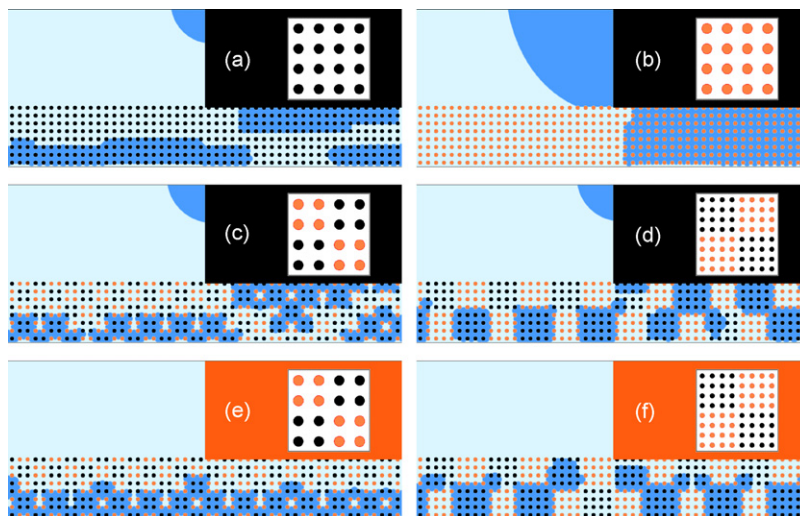


Fig. 7. The liquid water configuration for different fiber distributions and wettabilities. The average saturation is 45% and the porosity is $\sim 80\%$. The square insets at the top right corners show the distribution types of the hydrophobic carbon fibers (coated with Teflon). The black dots denote the hydrophilic fibers, while the orange dots denote the hydrophobic fibers. The blue regions denote the liquid water. The land surfaces from (a) to (d) are hydrophilic, while the land surfaces in (e) and (f) are hydrophobic. (For interpretation of the references to color in this figure legend, the reader is referred to the web version of the article.)

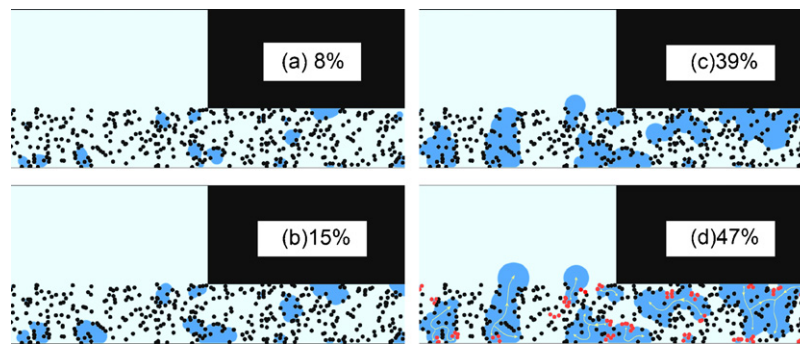


Fig. 8. The liquid water configuration and the evolution process for different average saturations: (a) 8%, (b) 15%, (c) 39%, and (d) 47%. The blue regions denote the liquid water droplets. All the fibers are hydrophilic. The red dots in (c) denote the fibers starting to form the initial condensation. (For interpretation of the references to color in this figure legend, the reader is referred to the web version of the article.)

growing up, such as the droplet at the bottom right corner. This is because that a high hydraulic pressure is required for liquid water to flow through the small pores. Another interesting phenomenon is that when the liquid water flows through the GDL into the flow channel, the nearby droplets will stop growing up. As shown in Fig. 8(c) and (d), all the droplets under the flow channel stop growing up when the liquid water intrudes into the flow channel. Most of the water droplets will encounter the dead ends in the GDL and occupy more space, especially at the regions under the land. This agrees with the pore-network modeling simulation of Sinha and Wang [38].

Fig. 8(d) shows the process of the movement paths of the liquid water. 21 red points (fibers with red color) indicate the initial positions of condensation occurring. But only 10 of them grow up. The lines and arrowheads show the routes and directions of the liquid water flow. The liquid water will flow through the big pores between fibers. This is because the curvature of the droplet at the big pore is smaller than that at the small pore, and therefore the pressure difference for liquid–gas interface movement in the big pore is also smaller than that in the small pore. Therefore, for a good design of GDL, the following two conditions are required: (a) there are some connected big pores from MPL to GDL, and (b) there are enough small hydrophobic pores to afford space for the reactant gas to flow.

The temperature gradient is neglected in the present analysis. This simplification induces an underestimation of the velocities of vapor condensation in the channel and the region nearby the land. If the temperature gradient exists in the cathode, the droplet would congregate where the temperature is lower for the same wettabilities of fiber surfaces.

4. Conclusions

Understanding the process of the liquid water droplet formation and transport in the GDL is a key to unraveling the origin and development of flooding. In the present paper, the equivalent capillary model of fiber-fence structure and lattice Boltzmann method are applied to simulate the micro-scale multiphase flow in the GDL. The possible contributors to liquid water configuration are discussed, such as capillary pressure, gravity and phase change. We also qualitatively discuss the effect of fiber distribution and spatial mixed-wettability distribution on the liquid water transport in the microstructure of the GDL. We delineate the fundamental process of the liquid water transport in the GDL. The main findings and conclusions are as follows:

(1) A positive hydraulic pressure is required for driving the liquid water to flow through the pores even for the large pores surrounded by hydrophilic fibers.

- (2) The pores under the rib land are easily blocked by liquid water due to the hydrophilic surface of the land and the high flow resistance of the liquid water moving into the flow channel.
- (3) The fraction of the hydrophobic fibers itself cannot describe the transport ability of the liquid water through the GDL. It is found that the hydrophobic treatment pattern plays an important role in the liquid water configuration.
- (4) After the liquid water flows through the GDL into the flow channel, the nearby droplets will almost stop grow up, where a gaseous flow path will be supplied.

Acknowledgments

This work was supported by the National Natural Science Foundation of China (90816025, 10672035, 10972050, 10721062), and “863” project 2007AA04Z405.

References

- [1] J.T. Gostick, M.W. Fowler, M.A. Ioannidis, M.D. Pritzker, Y.M. Volkovich, A. Sakars, *Journal of Power Sources* 156 (2006) 375–387.
- [2] P. Cheung, J.D. Fairweather, D.T. Schwartz, *Journal of Power Sources* 187 (2009) 487–492.
- [3] S. Basu, C.Y. Wang, K.S. Chen, *Journal of The Electrochemical Society* 156 (2009) B748–B756.
- [4] C. Hartnig, I. Manke, R. Kuhn, N. Kardjilov, J. Banhart, W. Lehnert, *Applied Physics Letters* 92 (2008) 134106.
- [5] C. Hartnig, I. Manke, R. Kuhn, S. Kleinau, J. Goebbels, J. Banhart, *Journal of Power Sources* 188 (2009) 468–474.
- [6] J. Nam, M. Kaviany, *International Journal of Heat and Mass Transfer* 46 (2003) 4595–4611.
- [7] F.Y. Zhang, X.G. Yang, C.Y. Wang, *Journal of the Electrochemical Society* 153 (2006) A225–A232.
- [8] C. Ziegler, D. Gerteisen, *Journal of Power Sources* 188 (2009) 184–191.
- [9] A. Bazylak, *International Journal of Hydrogen Energy* 34 (2009) 3845–3857.
- [10] M.F. Mathias, in: H.A.G. Wolf Vielstich, Arnold Lamm (Eds.), *Handbook of Fuel Cells—Fundamentals, Technology and Applications*, John Wiley & Sons, Ltd., New York, 2003.
- [11] A.L. Dicks, *Journal of Power Sources* 156 (2006) 128–141.
- [12] C. Lim, C.Y. Wang, *Electrochimica Acta* 49 (2004) 4149–4156.
- [13] P.K. Sinha, C.Y. Wang, *Chemical Engineering Science* 63 (2008) 1081–1091.
- [14] J. Benziger, J. Nehlsen, D. Blackwell, T. Brennan, J. Itescu, *Journal of Membrane Science* 261 (2005) 98–106.
- [15] S. Dutta, S. Shimpalee, J.W. Van Zee, *International Journal of Heat Mass and Transfer* 44 (2001) 2029–2042.
- [16] J.G. Pharoah, *Journal of Power Sources* 144 (2005) 77–82.
- [17] J. Park, X. Li, *Journal of Power Sources* 163 (2007) 853–863.
- [18] L. Jordan, A. Shukla, T. Behrsing, N. Avery, B. Muddle, M. Forsyth, *Journal of Power Sources* 86 (2000) 250–254.
- [19] H. Lee, J. Park, D. Kim, T. Lee, *Journal of Power Sources* 131 (2004) 200–206.
- [20] W.-K. Lee, J.W. Van Zee, A. Jena, K. Gupta, *Fuel Cell Seminar* (2004).
- [21] J. Bear, *Dynamics of Fluids in Porous Media*, Dover Publications, Inc., New York, 1988.
- [22] G.R. Mcnamara, G. Zanetti, *Physical Review Letters* 61 (1988) 2332–2335.
- [23] J. Park, M. Matsubara, X. Li, *Journal of Power Sources* 173 (2007) 404–414.
- [24] X.D. Niu, T. Munekata, S.-A. Hyodo, K. Suga, *Journal of Power Sources* 172 (2007) 542–552.

- [25] T. Koido, T. Furusawa, K. Moriyama, *Journal of Power Sources* 175 (2008) 127–136.
- [26] J. Park, X. Li, *Journal of Power Sources* 178 (2008) 248–257.
- [27] P.K. Sinha, P.P. Mukherjee, C.Y. Wang, *Journal of Materials Chemistry* 17 (2007) 3089–3103.
- [28] X. Shan, H. Chen, *Physical Review E* 49 (1994) 2941–2948.
- [29] P. Yuan, L. Schaefer, *Physics of Fluids* 18 (2006) 042101.
- [30] D.Y. Peng, D.B. Robinson, *Industrial Engineering Chemistry and Fundamentals* 15 (1976) 59–64.
- [31] N.S. Martys, H. Chen, *Physical Review E* 53 (1996) 743–750.
- [32] T.F. Fuller, J. Newman, *Journal of Electrochemical Society* 140 (1993) 1218–1225.
- [33] T.V. Nguyen, R.E. White, *Journal of Electrochemical Society* 140 (1993) 2178–2186.
- [34] X.Q. Yan, M. Hou, H.F. Zhang, F. Jing, P.W. Ming, B.L. Yi, *Journal of Power Sources* 1 (2006) 252–257.
- [35] E.C. Kumbur, K.Y. Sharp, M.M. Mench, *Journal of Power Sources* 2 (2007) 356–368.
- [36] R. Borup, M. Inbody, J. Davey, D. Wood, F. Garzon, J. Tafuya, J. Xie, S. Pacheco, DOE Hydrogen Program, FY, Progress Report, 2004.
- [37] E. Kimball, T. Whitaker, Y.G. Kevrekidis, J.B. Benziger, *AIChE Journal* 54 (2008) 1313–1332.
- [38] P.K. Sinha, C.Y. Wang, *Electrochimica Acta* 52 (2007) 7936–7945.